Graph Laplacian Tomography from Unknown Random Projections

Ronald. R. Coifman, Yoel Shkolnisky, Fred J. Sigworth and Amit Singer

***Abstract*—We introduce a graph Laplacian based algorithm for the tomography reconstruction of a planar object from its projections taken at random unknown directions. The algorithm is shown to successfully reconstruct the Shepp-Logan phantom from its noisy projections. Such a reconstruction algorithm is desirable for the structuring of certain biological proteins using cryo electron microscopy.**

I. Introduction

A standard problem in computerized tomography (CT) is reconstructing an object from samples of its projections. Focusing our attention to a planar object characterized by its density function $\rho(x,y)$, its Radon transform projection $P_\theta(t)$ is the line integral of ρ along parallel lines L inclined at an angle θ with distances t from the origin (see, e.g, [1]–[3])

$$\begin{aligned} P_\theta(t) &= \int_L \rho(x,y)ds \\ &= \iint_{-\infty}^{\infty} \rho(x,y)\delta(x\cos\theta + y\sin\theta - t)dx\,dy. \end{aligned} \tag{1}$$

The function ρ represents a property of the examined object which depends on the imaging modality. For example, ρ represents the X-ray attenuation coefficient in the case of X-ray tomography (CT scanning), the concentration of some radioactive isotope in PET scanning, or the refractive index of the object in ultrasound tomography.

Tomographic reconstruction algorithms estimate the function ρ from a finite set of samples of $P_\theta(t)$, assuming that the sampling points (θ,t) are known. See [4] for a survey of tomographic reconstruction methods. However, there are cases in which the projection angles are unknown, for example, when reconstructing certain biological proteins or other moving objects. In such cases, one is given samples of the projection function $P_{\theta_i}(t)$ for a finite but unknown set of angles $\{\theta_i\}$, and the problem at hand is to estimate the underlying function ρ without knowing the angle values. The sampling set for the parameter t is usually known and dictated by the physical setting of the acquisition process; for example, if the detectors are equally spaced then the values of t correspond to the location of the detectors along the detectors line, while the origin may be set at the center of mass.

In this paper we consider the reconstruction problem for the 2D parallel-beam model with unknown acquisition angles. Formally, we consider the following problem: Given N projection vectors $(P_{\theta_i}(t_1), P_{\theta_i}(t_2), \ldots, P_{\theta_i}(t_n))$ taken at unknown angles $\{\theta_i\}_{i=1}^N$ that were randomly drawn from the uniform distribution of $[0,2\pi]$ and $t_1, t_2, \ldots, t_n$ are fixed n equally spaced pixels in t, find the underlying density function $\rho(x,y)$ of the object.

A solution to this problem based on the moments of the projections was suggested and analyzed in [5], [6], where a simpler symmetric nearest neighbor algorithm was also described and tested numerically. Estimation of the projection angles is obtained from their ordering. This follows from the properties of the order statistics of uniformly distributed angles. Once the ordering is determined, the projection angles are estimated to be equally spaced on the unit circle. Thus, the problem boils down to sorting the projections with respect to their angles.

Our proposed algorithm sorts the projections by using the graph Laplacian [7], [8]. Graph Laplacians are widely

Ronald R. Coifman, Yoel Shkolnisky and Amit Singer are with the Department of Mathematics, Program in Applied Mathematics, Yale University, 10 Hillhouse Ave. PO Box 208283, New Haven, CT 06520-8283 USA.

Fred J. Sigworth is with the Department of Cellular and Molecular Physiology, Yale University School of Medicine, 333 Cedar Street, New Haven, CT 06520 USA.

emails: coifman-ronald@yale.edu, yoel.shkolnisky@yale.edu, fred.sigworth@yale.edu, amit.singer@yale.edu

used in machine learning for dimensionality reduction, semi-supervised learning and spectral clustering. However, their application to this image reconstruction problem seems to be new. Briefly speaking, an N by N matrix of weights related to the pairwise projection distances is constructed, followed by a computation of its first few eigenvectors. The eigenvectors reveal the correct ordering of the projections in a manner to be later explained. This algorithm may also be viewed as a generalization of the nearest-neighbor insertion algorithm [6] as it uses several weighted nearest neighbors at once. More importantly, the graph Laplacian incorporates all local pieces of information into a coherent global picture, eliminating the dependence of the outcome on any single local datum. Small local perturbations of the data points have almost no effect on the outcome. This global information is encoded in the first few smooth and slowly-varying eigenvectors, which depend on the entire dataset. Our numerical examples show that increasing the number of projections improves the performance of the sorting algorithm. We examine the influence of corrupting the projections by white Gaussian additive noise on the performance of the graph Laplacian sorting algorithm and its ability to reconstruct the underlying object. We find that applying classical filtering methods to de-noise the projection vectors, such as the translation invariant spin-cycle wavelet de-noising [9], gives successful reconstructions at even higher levels of noise.

This work was motivated by a similar problem in three dimensions, where a 3D object is to be reconstructed from its 2D line integral projections (X-ray transform) taken at unknown directions, as is the case in CryoEM microscopy [10]–[12]. Though there is no sense of order anymore, the graph Laplacian may be used to reveal the projection directions also in this higher dimensional case, as will be described in further details in a separate publication.

The organization of the paper is as follows. In Section II we survey graph Laplacians, which are being used in Section III for solving the tomography problem. The performance of the algorithm is demonstrated in Section IV. Finally, Section V contains some concluding remarks and a discussion of future extensions.

II. Graph Laplacians Sort Projections

Though graph Laplacians are widely used in machine learning for dimensionality reduction of high dimensional data, semi-supervised learning and spectral clustering, their usage in tomography is uncommon. For that reason, a self contained albeit limited description of graph Laplacians is included here. The presentation alternates between a general presentation of graph Laplacians and a specific consideration of their role in the tomography problem at hand. For a more detailed description of graph Laplacians and their applications the reader is referred to [7], [8], [13]–[15] (and references therein).

A. Spectral embedding

In the context of dimensionality reduction, high dimensional data points are described by a large number of coordinates n, and a reduced representation that uses only a few effective coordinates is wanted. Such a low-dimensional representation is sought to preserve properties of the high-dimensional dataset, such as, local neighborhoods [13], [16], geodesic distances [17] and diffusion distances [7]. It is often assumed that the data points approximately lie on a low dimensional manifold, typically a non-linear one. In such a setting, the N data points $x_1, \ldots, x_N$ are viewed as points in the ambient Euclidean space $\mathbb{R}^n$, while it is assumed that they are restricted to an intrinsic low dimensional manifold $\mathcal{M}$. In other words, $x_1, \ldots, x_N \in \mathcal{M} \subset \mathbb{R}^n$ and $d = \dim \mathcal{M} \ll n$. We assume that the structure of the manifold $\mathcal{M}$ is unknown, and one can only access the data points $x_1, \ldots, x_N$ as points in $\mathbb{R}^n$. Fitting the data points using linear methods such as linear regression, least square approximation or principal component analysis, to name a few, usually performs poorly when the manifold is non-linear. The graph Laplacian, however, is a non-linear method that overcomes the shortcomings of the linear methods.

In our tomography problem, each data point corresponds to a projection at some fixed angle θ_i, sampled at n equally spaced points in the t direction

$$x_i = \left(P_{\theta_i}(t_1), P_{\theta_i}(t_2), \ldots, P_{\theta_i}(t_n)\right), \quad i = 1, 2, \ldots, N. \tag{2}$$

The vector that corresponds to each projection is viewed as a point $x_i \in \mathbb{R}^n$; however, all points x_i lie on a closed curve $P \subset \mathbb{R}^n$ where

$$P(\theta) = \left(P_\theta(t_1), P_\theta(t_2), \ldots, P_\theta(t_n)\right), \quad \theta \in [0, 2\pi). \tag{3}$$

The closed curve P is a one dimensional manifold of $\mathbb{R}^n$ ($d = 1$) parameterized by the projection angle θ. The exact shape of the curve depends on the underlying imaged object $\rho(x, y)$, so different objects give rise to different curves. The particular curve P is unknown to us, because the object $\rho(x, y)$ is unknown. However, recovering the curve, or, in general, the manifold, from a sufficiently large number of data points sounds plausible.

In practice, the manifold is recovered by constructing the graph Laplacian and computing its first few eigenvectors. The starting point is constructing an $N \times N$ weight matrix W using a suitable semi-positive kernel k as follows

$$W_{ij} = k\left(\frac{\|x_i - x_j\|^2}{2\varepsilon}\right), \quad i, j = 1, \ldots, N, \tag{4}$$

where $\|\cdot\|$ is the Euclidean norm of the ambient space $\mathbb{R}^n$ and $\varepsilon > 0$ is a parameter known as the bandwidth of the kernel. A popular choice for the kernel function is $k(x) = \exp(-x)$, though other choices are also possible [7], [8]. The weight matrix W is then normalized to be row stochastic, by dividing it by a diagonal matrix D whose elements are the row sums of W

$$D_{ii} = \sum_{j=1}^{N} W_{ij}. \tag{5}$$

The (negative defined) normalized graph Laplacian L is then given by

$$L = D^{-1}W - I, \tag{6}$$

where I is the $N \times N$ identity matrix. There exist normalizations other than the row stochastic one; the choice of normalization and the differences between them are addressed below.

The row stochastic matrix $D^{-1}W$ has a complete set of eigenvectors ϕ_i and eigenvalues λ_i

$$1 = \lambda_0 > \lambda_1 \geq \ldots \geq \lambda_i \geq \lambda_{i+1} \geq \ldots \geq \lambda_{N-1} \geq 0,$$

and the first eigenvector is constant, that is, $\phi_0 = (1, 1, \ldots, 1)^T$. The remaining eigenvectors $\phi_1, \ldots, \phi_k$, for some $k \ll N$, define a k-dimensional non-linear spectral embedding of the data

$$x_i \mapsto (\phi_1(i), \phi_2(i), \ldots, \phi_k(i)), \quad i = 1, \ldots, N. \tag{7}$$

It is sometimes advantageous to incorporate the eigenvalues into the embedding by defining

$$x_i \mapsto \left(\lambda_1^t \phi_1(i), \lambda_2^t \phi_2(i), \ldots, \lambda_k^t \phi_k(i)\right), \quad i = 1, \ldots, N,$$

for some $t \geq 0$ [7].

B. Uniform datasets and the Laplace-Beltrami operator

The embedding (7) has many nice properties and we choose to emphasize only one of them, namely the intimate connection between the graph Laplacian matrix L and the continuous Laplace-Beltrami operator $\Delta_{\mathcal{M}}$ of the manifold $\mathcal{M}$. This connection is manifested in the following theorem [18]: if the data points $x_1, x_2, \ldots, x_N$ are independently uniformly distributed over the manifold $\mathcal{M}$ then with high probability

$$\frac{1}{\varepsilon}\sum_{j=1}^{N} L_{ij} f(x_j) = \frac{1}{2}\Delta_{\mathcal{M}} f(x_i) + O\left(\frac{1}{N^{1/2}\varepsilon^{1/2+d/4}}, \varepsilon\right), \tag{8}$$

where $f : \mathcal{M} \mapsto \mathbb{R}$ is any smooth function. The approximation in (8) incorporates two error terms: a bias term of $O(\varepsilon)$ which is independent of N and a variance term of $O\left(N^{-1/2}\varepsilon^{-(1/2+d/4)}\right)$. The theorem implies that the discrete operator L converges pointwise to the continuous Laplace-Betrami operator in the limit $\varepsilon \to 0$ and $N \to \infty$ as long as $N\varepsilon^{1+d/2} \to \infty$.

In other words, applying the discrete operator L to a smooth function sampled at the data points approximates the Laplace-Beltrami of that function evaluated at those data points. Moreover, the eigenvectors of the graph Laplacian L approximate the eigenfunctions of $\Delta_{\mathcal{M}}$ that correspond to homogenous Neumann boundary condition (vanishing normal derivative) in the case that the manifold has a boundary [19].

This connection between the graph Laplacian and the Laplace-Beltrami operator sheds light on the spectral embedding (7). For example, consider a closed curve $P \subset \mathbb{R}^n$ of length L parameterized by its arclength s. The Laplace-Beltrami Δ_P of P is simply the second order derivative with respect to the arclength, $\Delta_P f(s) = f''(s)$. The eigenfunctions of Δ_P satisfy

$$f''(s) = -\lambda f(s), \quad s \in (0, L) \tag{9}$$

with the periodic boundary conditions

$$f(0) = f(L), \quad f'(0) = f'(L). \tag{10}$$

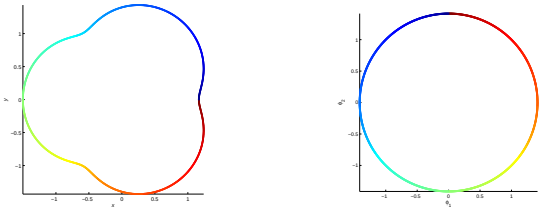

(a) (b)

Fig. 1: Uniformly sampled epitrochoid and its spectral embedding: (a) An epitrochoid that corresponds to $R = 1$, $r = 1/3$, $d = 1/6$. Points are equally spaced in arc-length. (b) Embedding the epitrochoid into the eigenvectors (ϕ_1, ϕ_2) of the graph Laplacian.

q

The first eigenfunction is the constant function $\phi_0(s) = 1$ with eigenvalue $\lambda_0 = 0$. The remaining eigenfunctions are $\{\cos(2\pi ms/L), \sin(2\pi ms/L)\}_{m=1}^{\infty}$ with corresponding degenerated eigenvalues $\lambda_m = 4\pi^2 m^2/L^2$ of multiplicity 2. It follows that embedding $P \subset \mathbb{R}^n$ using the first two non-trivial eigenfunctions results in the unit circle in the plane

$$P(s) \mapsto (\cos(2\pi s/L), \sin(2\pi s/L)), \quad s \in [0, L]. \tag{11}$$

For data points $x_1, \ldots, x_N$ that are uniformly distributed over the curve P, the first two non-trivial eigenvectors of the graph Laplacian are approximately $\cos(2\pi s/L)$ and $\sin(2\pi s/L)$ and the embedding (7) reads

$$P(s_i) = x_i \mapsto (\phi_1(i), \phi_2(i)) \approx (\cos(2\pi s_i/L), \sin(2\pi s_i/L)), \tag{12}$$

for $i = 1, \ldots, N$. Due to the multiplicity of the eigenvalues, the computed eigenvectors can be any orthogonal 2×2 linear transformation of ϕ_1 and ϕ_2. The specific orthogonal combination depends on the numerical procedure used to compute the eigenvectors. Thus, the embedding is unique up to an arbitrary rotation and possibly a reflection (orientation). Figure 1b shows that the graph Laplacian embedding of data points equally spaced with respect to arc-length along the epitrochoid in Fig. 1a is indeed a circle.

The two dimensional embedding (12) reveals the ordering of the data points x_i along the curve P. Going back to the tomography problem, the graph Laplacian embedding of the projection vectors (2) reveals their true ordering. The last statement is indeed correct, but we should exercise more carefulness in its justification.

The graph Laplacian approximates the Laplace-Beltrami operator if the data points are uniformly distributed over the manifold. However, this is not the case in our tomography problem. Even though the projection angles are uniformly distributed on the unit circle, the projection vectors are not uniformly distributed over the curve in $\mathbb{R}^n$ on which they lie with respect to its arc-length. To this end, we examine the relationship between the probability density function $p_\Theta(\theta)$ of the projection angle θ and the probability density function $p_S(s)$ of the projection vectors over the curve P. This relationship is given by

$$p_\Theta(\theta)\, d\theta = p_S(s)\, ds, \tag{13}$$

for infinitesimals arclength ds and angle $d\theta$, because $P : S^1 \mapsto \mathbb{R}^n$ conserves the number of mapped points. The uniform distribution of the angle θ means $p_\Theta(\theta) = \dfrac{1}{2\pi}$, hence

$$p_S(s) = p_\Theta(\theta) \left(\frac{ds}{d\theta}\right)^{-1} = \frac{1}{2\pi} \left\| \frac{dP}{d\theta} \right\|^{-1}. \tag{14}$$

The density $p_S(s)$ depends on the specific object $\rho(x, y)$ through P and is usually not uniform, because $\left\| \dfrac{dP}{d\theta} \right\|$ is not constant. Note that $\left\| \dfrac{dP}{d\theta} \right\|$ is well defined for every finite number of pixels n. The limit $n \to \infty$ is subtle, because it may happen that $\left\| \dfrac{dP}{d\theta} \right\| \to \infty$. In such a case, the curve $P_\theta(t) \subset L^2(\mathbb{R})$ parameterized by $\theta \in [0, 2\pi)$ has no well defined length. This happens, for example, for the ellipse given by $\rho(x, y) = 1$ for $x^2/A^2 + y^2/B^2 \leq 1$ and $\rho(x, y) = 0$ otherwise. The jump discontinuity at the boundary of the ellipse leads to a square-root singularity in $P_\theta(t)$, which in turn yields a behavior of the form $\|P_{\theta_2} - P_{\theta_1}\|^2 = O\left(|\theta_2 - \theta_1| \log |\theta_2 - \theta_1|\right)$ as $|\theta_2 - \theta_1| \to 0$.

C. Non-uniform densities and the Fokker-Planck operator

When data points are distributed over a manifold $\mathcal{M}$ according to a non-uniform density $p(x)$, their graph Laplacian does not approximate the Laplace-Beltrami operator, but rather a different differential operator, known as the backward Fokker-Planck operator $\mathcal{L}$, [8], [20]

$$\mathcal{L} f = \Delta_{\mathcal{M}} f - \nabla U \cdot \nabla f, \tag{15}$$

where $U(x) = -2\log p(x)$ is the potential function. Thus, the more general form of (8) is

$$\frac{1}{\varepsilon}\sum_{j=1}^{N} L_{ij} f(x_j) \approx \frac{1}{2}\mathcal{L}f(x_i). \tag{16}$$

Note that the Fokker-Planck operator $\mathcal{L}$ coincides with the Laplace-Beltrami operator in the case of a uniform distribution for which the potential function U is constant, so its gradient vanishes.

The Fokker-Planck operator has a complete set of eigenfunctions and eigenvalues. In particular, when the manifold is a closed curve P of length L, the eigenfunctions satisfy

$$f'' - U'f' = -\lambda f \tag{17}$$

with the periodic boundary conditions

$$f(0) = f(L), \quad f'(0) = f'(L). \tag{18}$$

We rewrite the eigenfunction problem (17) as a Sturm-Liouville problem

$$\left(e^{-U} f'\right)' + \lambda e^{-U} f = 0. \tag{19}$$

Although the eigenfunctions are no longer the sine and cosine functions, it follows from the classical Sturm-Liouville theory of periodic boundary conditions and positive coefficients ($e^{-U(s)} = p_S^2(s) > 0$) [21] that the embedding consisting of the first two non-trivial eigenfunctions ϕ_1, ϕ_2 of (17)–(18) also circles the origin exactly once in a manner that the angle is monotonic. In other words, upon writing the embedding in polar coordinates (r, φ)

$$P(s) \mapsto (\phi_1(s), \phi_2(s)) = r(s)e^{i\varphi(s)}, \quad s \in [0, L] \tag{20}$$

the argument $\varphi(s)$ is a monotonic function of s, with $\varphi(0) = 0$, $\varphi(L) = 2\pi$. Despite the fact that the explicit form of the eigenfunctions is no longer available, the graph Laplacian embedding reveals the ordering of the projections through the angle φ_i attached to x_i. Figs. 2a and 2b show a particular embedding of a curve into the eigenfunctions of the Fokker-Planck operator. The embedding is no longer a circle as it depends on the geometry of the curve.

D. Density invariant graph Laplacian

What if data points are distributed over $\mathcal{M}$ with some non-uniform density, and we still want to approximate the Laplace-Beltrami operator on $\mathcal{M}$ instead of the Fokker-Planck operator? This can be achieved by replacing the row stochastic normalization in (5) and (6) by the so-called density invariant normalization. Such a normalization is described in [8] and leads to the density invariant graph Laplacian. This normalization is obtained as follows. First, normalize both rows and columns of W to form a new weight matrix $\tilde{W}$

$$\tilde{W} = D^{-1} W D^{-1}, \tag{21}$$

where D is the diagonal matrix (5) whose elements are the row sums of W. Next, normalize the new weight matrix $\tilde{W}$ to be row stochastic by dividing it by a diagonal matrix $\tilde{D}$ whose elements are the row sums of $\tilde{W}$

$$\tilde{D}_{ii} = \sum_{j=1}^{N} \tilde{W}_{ij}. \tag{22}$$

Finally, the (negative defined) density invariant graph Laplacian $\tilde{L}$ is given by

$$\tilde{L} = \tilde{D}^{-1}\tilde{W} - I. \tag{23}$$

The density invariant graph Laplacian $\tilde{L}$ approximates the Laplace-Beltrami operator with $\tilde{L}$ replacing L in (8) [8], even when the data points are non-uniformly distributed over $\mathcal{M}$. Therefore, embedding non-uniformly distributed data points over a closed curve P using the density-invariant graph Laplacian results in a circle given by (11)–(12). As mentioned before, although θ is uniformly distributed in $[0, 2\pi)$, the arclength s is not uniformly distributed in $[0, L]$, but rather has some non-constant density $p_S(s)$. It follows that the embedded points that are given by (12) are non-uniformly distributed on the circle. Nonetheless, the embedding reveals the ordering of the projection vectors. Figures 3b and 3d show

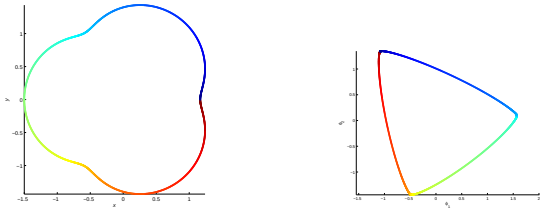

(a) (b)

Fig. 2: Density dependent embedding: (a) An epitrochoid that corresponds to $R = 1$, $r = 1/3$, $d = 1/6$. Points are equally spaced in $\theta \in [0, 2\pi)$. (b) Embedding the epitrochoid into the eigenvectors (ϕ_1, ϕ_2) of the graph Laplacian.

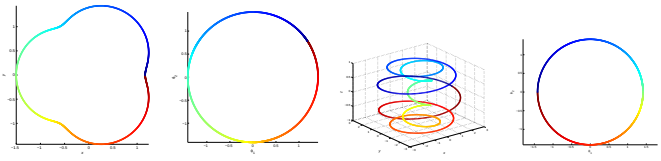

(a) (b) (c) (d)

Fig. 3: Density invariant embedding of the epitrochoid and a closed helix: (a) An epitrochoid that corresponds to $R = 1$, $r = 1/3$, $d = 1/6$. Points are equally spaced in $\theta \in [0, 2\pi)$. (b) Embedding the epitrochoid into the eigenvectors (ϕ_1, ϕ_2) of the density invariant graph Laplacian. (c) A closed helix in $\mathbb{R}^3$. Points are non-equally spaced in arc-length. (d) Embedding the closed helix into the eigenvectors (ϕ_1, ϕ_2) of the density invariant graph Laplacian.

the embedding of the epitrochoid (Fig. 3a) and a closed helix in $\mathbb{R}^3$ (Fig. 3c) into the first two eigenfunctions of the Laplace-Beltrami operator, obtained by applying the density-invariant normalization.

The graph Laplacian integrates local pieces of information into a global consistent picture. Each data point interacts only with a few of its neighbors, or a local cloud of points, because the kernel is rapidly decaying outside a neighborhood of size $\sqrt{\varepsilon}$. However, the eigenvector computation involves the entire matrix and glues those local pieces of information together.

III. Recovering the projection angles

Once the projection vectors are sorted, the values of the projection angles $\theta_1, \ldots, \theta_N$ need to be estimated. Since the projection angles are uniformly distributed over the circle, we estimate the sorted projection angles

$$\theta_{(1)} < \theta_{(2)} < \ldots < \theta_{(N)}$$

by equally spaced angles $\bar{\theta}_{(k)}$ (the bar indicates that these are estimated angle values rather than true values)

$$\bar{\theta}_{(k)} = \frac{2\pi k}{N}, \; k = 1, \ldots, N. \tag{24}$$

Due to rotation invariance, we fix $\theta_{(N)} = 2\pi$. The remaining $N-1$ random variables $\theta_{(k)}$ $(k = 1, \ldots, N-1)$ are known as the kth order statistics [22] and their (marginal) probability density functions $p_{\theta_{(k)}}(\theta)$ are given by

$$\frac{(N-1)!}{2\pi(k-1)!(N-1-k)!}\left(\frac{\theta}{2\pi}\right)^{k-1}\left(1-\frac{\theta}{2\pi}\right)^{N-1-k},$$

for $\theta \in [0, 2\pi]$. The mean value and variance of $\theta_{(k)}$ are

$$\mathbb{E}\theta_{(k)} = \frac{2\pi k}{N}, \qquad \operatorname{Var}\theta_{(k)} = \frac{4\pi^2 k(N-k)}{(N+1)N^2}.$$

Thus, the equally spaced estimation (24) of the kth order statistics is in fact the mean value estimation, and the mean square error (MSE) given by $\operatorname{Var}\theta_{(k)}$ is maximal for $k = \lfloor N/2 \rfloor$

$$\operatorname{Var}\theta_{(\lfloor N/2 \rfloor)} \sim \frac{\pi^2}{N} + O\left(\frac{1}{N^2}\right).$$

The MSE vanishes as the number of data points $N \to \infty$, and the typical estimation error is $O(1/\sqrt{N})$.

Now that the projection angles have been estimated, any classical tomography algorithm may be applied to reconstruct the image. The image can be reconstructed either from the entire set of N projection vectors, or it can be reconstructed from a smaller subset of them. Given a set of mN projection vectors, where m is an over-sampling factor, we first sort all mN angles

$$\theta_{(1)} < \theta_{(2)} < \ldots < \theta_{(mN)}$$

using the density-invariant graph Laplacian, but use only N of them (every mth projection)

$$\theta_{(m)} < \theta_{(2m)} < \ldots < \theta_{(mN)}$$

for the image reconstruction. The effect of sub-sampling is similarly understood in terms of the order statistics.

Note that the symmetry of the projection function (1)

$$P_\theta(t) = P_{\theta+\pi}(-t)$$

practically doubles the number of projections. For every given projection vector $P_{\theta_i}(t)$ that corresponds to an unknown angle θ_i we create the projection vector

$$P_{\theta_i'}(t) = P_{\theta_i}(-t) \tag{25}$$

that correspond to the unknown angle $\theta_i' = \theta_i + \pi$.

The reconstruction algorithm is summarized in Algorithm 1. Note that in steps 2 and 3 of Algorithm 1 the graph Laplacian L can be used instead of $\tilde{L}$.

IV. Numerical examples and noise tolerance

We applied to above algorithm to the reconstruction of the two-dimensional Shepp-Logan phantom, shown in Fig. 4a, from its projections at random angles. The results are illustrated in Figs. 4a–4d.

Algorithm 1 Reconstruction from random orientations

Require: Projection vectors $P_{\theta_i}(t_1,\ldots,t_n)$, $i = 1,2,\ldots,mN$

1: Double the number of projection vectors to $2mN$ using (25).
2: Construct the density invariant graph Laplacian $\tilde{L}$ following (4)-(5), (21)-(23).
3: Compute the first two non-trivial eigenvectors of $\tilde{L}$: ϕ_1, ϕ_2.
4: Sort P_{θ_i} according to φ_i that satisfies $(r_i\cos\varphi_i, r_i\sin\varphi_i) = (\phi_1(i), \phi_2(i))$ to get the sorted projections $P_{\theta_{(i)}}$.
5: Reconstruct the image using N projection vectors $P_{\theta_{(2mi)}}$ that correspond to estimated angles $\bar{\theta}_{(2mi)} = 2\pi i/N$, $i = 1,\ldots,N$.

The figures were generated as follows. We set $N = 256$, and for each over-sampling factor $m = 4, 8, 16$, we generated mN uniformly distributed angles in $[0, 2\pi]$, denoted $\theta_1,\ldots,\theta_{mN}$. Then, for each θ_i, we evaluated the analytic expression of the Radon transform of the Shepp-Logan phantom [2] at $n = 500$ equally spaced points between -1.5 and 1.5. That is, each P_{θ_i} is a vector in $\mathbb{R}^{500}$. We then applied Algorithm 1 and reconstructed the Shepp-Logan phantom using $N = 256$ projections. The results are presented in Figs. 4b–4d for $m = 4, 8, 16$, respectively. The density invariant graph-Laplacian (Algorithm 1) was constructed using the kernel $k(x) = e^{-x}$ with $\varepsilon = 0.05$. The dependence of the algorithm on ε is demonstrated below. All tests were implemented in Matlab. The Radon transform was inverted using Matlab's `iradon` function with spline interpolation and a hamming filter.

Note that Figs. 4b–4d exhibit an arbitrary rotation, and possibly a reflection as is the case in Fig. 4c, due to the random orthogonal mixing of the eigenfunctions ϕ_1 and ϕ_2 that consists of merely rotations and reflections.

A. Choosing ε

For the reconstructions in Figs. 4b–4d we used $\varepsilon = 0.05$. According to (8), in general, the value of ε should be chosen to balance the bias term that calls for small ε with the variance term that calls for large ε. In practice, however, the value of ε is set such that for each projection P_{θ_i} there are several neighboring projections P_{θ_j} for which W_{ij} in (4) are non-negligible. Figures 5a-5h depict the dependence of the quality of reconstruction on the value of ε. We conclude that the algorithm is stable with respect to ε in the sense that high quality reconstructions are obtained when ε is changed by as many as two orders of magnitude, from $5\cdot10^{-4}$ to $7.5\cdot10^{-2}$.

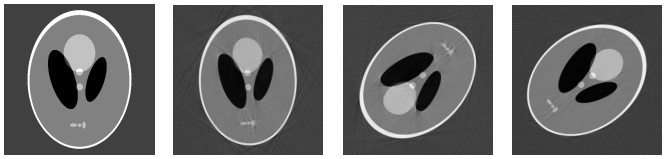

(a) Original Shepp-Logan phantom (b) $mN = 1024$ (c) $mN = 2048$ (d) $mN = 4096$

Fig. 4: Reconstructing the Shepp-Logan phantom from its random projections while using the symmetry of the Radon transform. $N = 256$.

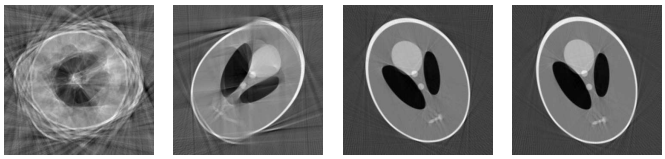

(a) $\varepsilon = 10^{-4}$ (b) $\varepsilon = 3\cdot10^{-4}$ (c) $\varepsilon = 5\cdot10^{-4}$ (d) $\varepsilon = 10^{-3}$

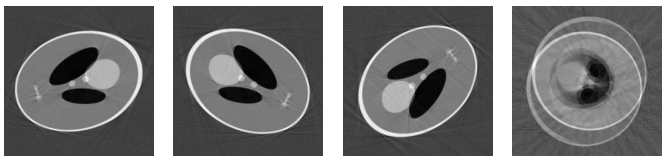

(e) $\varepsilon = 10^{-2}$ (f) $\varepsilon = 5\cdot10^{-2}$ (g) $\varepsilon = 7.5\cdot10^{-2}$ (h) $\varepsilon = 10^{-1}$

Fig. 5: Reconstructing the Shepp-Logan phantom from its random projections for different values of ε (increasing from (a) to (h)). All reconstructions use $N = 256$, $mN = 4096$, and $n = 500$ pixels per projection. High quality reconstructions are obtained for a wide range of ε values.

The value of ε can also be chosen in an automated way without manually verifying the reconstruction quality and without computing the eigenvectors of the graph Laplacian matrix. Following [23], we use a logarithmic scale to plot the sum of the N^2 weight matrix elements

$$\sum_{i,j} W_{ij}(\varepsilon) = \sum_{ij} \exp\left\{-\|x_i - x_j\|^2/2\varepsilon\right\} \qquad (26)$$

against ε (Fig 6). As long as the statistical error in (8) is small,

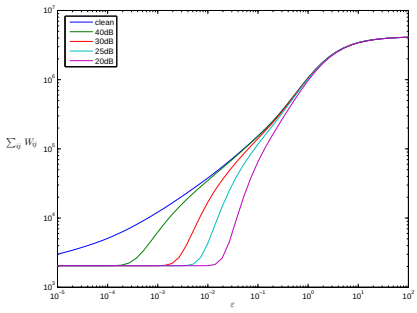

Fig. 6: Logarithmic scale plot of $\sum_{i,j=1}^{N} W_{ij}(\varepsilon)$ against ε for various levels of noise. The top (Blue) curve corresponds to noiseless projections.

the sum (26) is approximated by its mean value integral

$$\sum_{ij} \exp\left\{-\|x_i - x_j\|^2/2\varepsilon\right\} \tag{27}$$
$$\approx \frac{N^2}{\mathrm{vol}^2(\mathcal{M})} \int_{\mathcal{M}}\int_{\mathcal{M}} \exp\left\{-\|x-y\|^2/2\varepsilon\right\}\, dx\, dy,$$

where $\mathrm{vol}(\mathcal{M})$ is the volume of the manifold $\mathcal{M}$ and assuming uniformly distributed data points. For small values of ε, we approximate the narrow Gaussian integral

$$\int_{\mathcal{M}} \exp\left\{-\|x-y\|^2/2\varepsilon\right\}\, dx \tag{28}$$
$$\approx \int_{\mathbb{R}^d} \exp\left\{-\|x-y\|^2/2\varepsilon\right\}\, dx = (2\pi\varepsilon)^{d/2},$$

because the manifold looks locally like its tangent space $\mathbb{R}^d$. Substituting (28) in (27)-(26) gives

$$\sum_{i,j} W_{ij}(\varepsilon) \approx \frac{N^2}{\mathrm{vol}(\mathcal{M})} (2\pi\varepsilon)^{d/2},$$

or equivalently, upon taking the logarithm

$$\log\left(\sum_{i,j} W_{ij}(\varepsilon)\right) \approx \frac{d}{2}\log\varepsilon + \log\left(\frac{N^2\,(2\pi)^{d/2}}{\mathrm{vol}(\mathcal{M})}\right), \tag{29}$$

which means that the slope of the logarithmic scale plot is $d/2$. In the limit $\varepsilon \to \infty$, $W_{ij} \to 1$, so $\sum_{ij} W_{ij} \to N^2$. On the other hand, as $\varepsilon \to 0$, $W_{ij} \to \delta_{ij}$, so $\sum_{ij} W_{ij} \to N$. Those two limiting values assert that the logarithmic plot cannot be linear for all values of ε. In the linearity region, both statistical and bias errors are small, therefore, it is desirable to choose ε from that region.

In Fig 6, the top (Blue) curve corresponds to noiseless projection data points. The slope of that curve in the region of linearity, $10^{-3} \le \varepsilon \le 10^{-1}$, is approximately 0.5 as expected from data points that lie on a curve by (29) with $d = 1$.

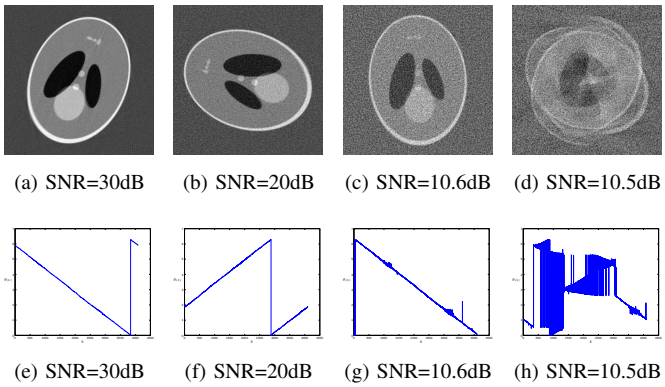

(a) SNR=30dB (b) SNR=20dB (c) SNR=10.6dB (d) SNR=10.5dB

(e) SNR=30dB (f) SNR=20dB (g) SNR=10.6dB (h) SNR=10.5dB

Fig. 7: *Top*: Reconstructing the Shepp-Logan phantom from its random projections that were corrupted by different levels of additive white noise. *Bottom*: Projection angles as estimated by the graph Laplacian sorting algorithm against their true value for the same levels of noise. The jump discontinuity is due to the rotation invariance of the problem. Reflection flips the slope to -1. ($mN = 4096, N = 256, n = 500$).

B. Noise tolerance

The effect of additive noise on the reconstruction is depicted in Figs. 7a–7d. For each figure, we randomly drew 4096 angles from a uniform distribution, computed the projections of the Shepp-Logan phantom corresponding to those angles and added noise to the computed projections. The noise was Gaussian with zero mean and a standard deviation that satisfied

$$\text{SNR [dB]} = 10\log_{10}\left(\frac{\mathrm{Var}\, S}{\mathrm{Var}\,\delta}\right),$$

where S is the array of the noiseless projections and δ is a realization of the noise. As before, once applying the algorithm, the images were reconstructed from $N = 256$ projections.

The reconstruction algorithm performs well above $\approx$ 10.6dB and performs poorly below this SNR value. As was pointed out in [5], this phenomenon is related to the threshold effect in non-linear parameter estimation [24], [25] that predicts a sharp transition in the success rate of detecting and estimating the signal from its noisy measurements as a function of the SNR. The manifestation of this phenomena in our case is that the distances in (4) become meaningless above a certain level of noise. Figures 7c and 7d demonstrate the breakdown of the algorithm when the SNR decreases by just 0.1dB. Figures 7e-7h demonstrate the same breakdown

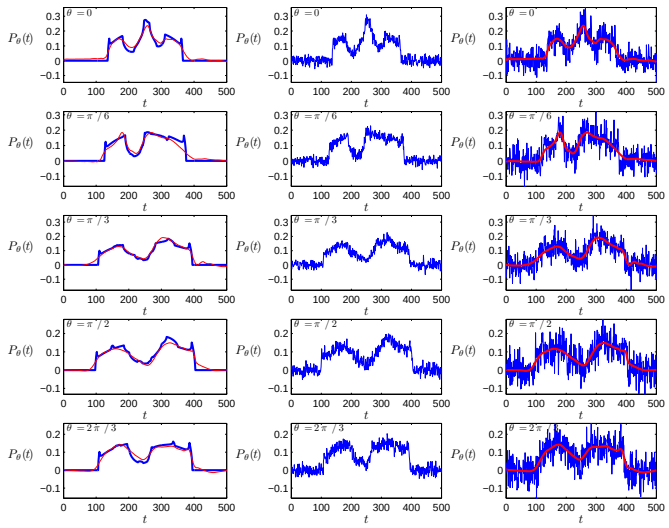

Fig. 8: Five different projections that differ by $\Delta\theta = \pi/6$ (left column, blue thick curve), their noisy version at 10.6dB (center column) and their noisy version at 2.0dB (right column). The red curves (right column and left column) correspond to applying the hard thresholding full spin-cycle de-noising algorithm with Daubechies 'db2' wavelets to the 2.0dB noisy projections of the right column.

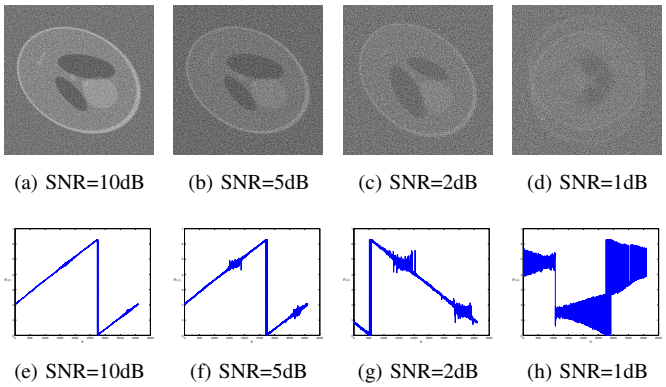

Fig. 9: *Top*: Reconstructing the Shepp-Logan phantom from its random projections that were corrupted by additive white noise by first spin-cycle filtering the projections. Main features of the phantom are reconstructed even at 2.0dB. *Bottom*: Projection angles as estimated by the graph Laplacian sorting algorithm with spin-cycled de-noised projections against their true value for different levels of noise. ($mN = 4096, N = 256, n = 500$)

by comparing the estimated projection angles with their true value. Figure 8 shows five different projections $P_{\theta_i}(t)$ separated by $\theta_{i+1} - \theta_i = \pi/6$ (left column, thick blue curve) and their noisy realizations at 10.6dB (center column), gauging the level of noise that can be tolerated.

The threshold effect can also be understood by Fig 6, where it is shown that higher levels of noise result in higher slope values, rendering larger empirical dimensions. In other words, adding noise thickens the curve $P \subset \mathbb{R}^n$ and effectively enlarges the dimensionality of the data. The graph Laplacian treats the data points as if they lie on a surface rather than a curve and stumbles upon the threshold effect.

The threshold point can be pushed down by initially de-noising the projections and constructing the graph Laplacian using the de-noised projections rather than the original noisy ones. In practice, we used the fast $O(n \log n)$ implementation of the full translation invariant wavelet spin-cycle algorithm [9] with Daubechies wavelets 'db2' of length 4 combined with hard thresholding the wavelet coefficients at $\sigma\sqrt{2 \log n}$, where $\sigma = \sqrt{\mathrm{Var}\,\delta / \mathrm{Var}\,S}$. Using this classical non-linear filtering method we were able to push down the threshold point from 10.6dB to 2.0dB as illustrated in Figures 9a-9h. Samples of spin-cycled de-noised projections (originally 2.0dB) are shown in Figure 8 in red.

V. Summary and Discussion

In this paper we introduced a graph Laplacian based algorithm for imaging a planar object given its projections at random unknown directions. The graph Laplacian is widely used nowadays in machine learning and high dimensional data analysis, however, its usage in tomography seems to be new. The graph Laplacian embeds the projection functions into a closed planar curve from which we estimate the projection angles. The graph Laplacian ensembles local projection similarities into a global embedding of the data. In that respect, our algorithm may be viewed as the natural generalization of the nearest neighbor algorithm of [5], [6].

We tested the graph Laplacian reconstruction algorithm for the Shepp-Logan phantom and examined its tolerance to noise. We observed the threshold effect and were able to improve the tolerance to noise by constructing a graph Laplacian based on de-noised projections. Our success in pushing down the threshold limit using the wavelets spin-cycle algorithm suggests that more sophisticated filtering techniques may tolerate even higher levels of noise. In particular, we speculate that

filtering the entire set of projection vectors all together, rather than one at a time, using neighborhood filters [26], non-local means [27] and functions adapted kernels [28], may push down the threshold even further. The original non-noisy projection vectors have similar features or building blocks (e.g., peaks, jumps, quiet regions, etc.) when the underlying imaged object is not too complex. We expect better recovery of those features when averaging similar slices across many different projections.

The reconstruction of a three-dimensional object from its projections taken at random unknown directions, which is motivated by CryoEM microscopy of biological proteins, will be the subject of a separate publication.

REFERENCES

[1] S. R. Deans, *The Radon Transform and Some of Its Applications*, revised ed. Krieger Publishing Company, 1993.

[2] A. C. Kak and M. Slaney, *Principles of Computerized Tomographic Imaging*, ser. Classics in Applied Mathematics. SIAM, 2001.

[3] F. Natterer, *The Mathematics of Computerized Tomography*, ser. Classics in Applied Mathematics. SIAM: Society for Industrial and Applied Mathematics, 2001.

[4] F. Natterer and F. Wûbbeling, *Mathematical Methods in Image Reconstruction*, 1st ed., ser. Monographs on Mathematical Modeling and Computation. SIAM: Society for Industrial and Applied Mathematics, 2001.

[5] S. Basu and Y. Bresler, "Feasibility of tomography with unknown view angles," *IEEE Transactions on Image Processing*, vol. 9, no. 6, pp. 1107–1122, June 2000.

[6] ——, "Uniqueness of tomography with unknown view angles," *IEEE Transactions on Image Processing*, vol. 9, no. 6, pp. 1094–1106, June 2000.

[7] R. R. Coifman and S. Lafon, "Diffusion maps," *Applied and Computational Harmonic Analysis*, vol. 21, no. 1, pp. 5–30, July 2006.

[8] S. Lafon, "Diffusion maps and geometric harmonics," Ph.D. dissertation, Yale University, 2004.

[9] R. R. Coifman and D. Donoho, "Translation invariant de-noising," in *Wavelets in Statistics*, A. Antoniadis and G. Oppenheim, Eds. New York: Springer, 1995, pp. 125–150.

[10] J. Frank, *Three-Dimensional Electron Microscopy of Macromolecular Assemblies*. Academic, 1996.

[11] P. Doerschuk and J. E. Johnson, "Ab initio reconstruction and experimental design for cryo electron microscopy," *IEEE Transactions on Information Theory*, vol. 46, no. 5, pp. 1714–1729, 2000.

[12] Q.-X. Jiang, E. C. Thrower, D. W. Chester, B. E. Ehrlich, and F. J. Sigworth, "Three-dimensional structure of the type 1 inositol 1,4,5-trisphosphate receptor at 24A resolution," *EMBO J.*, vol. 21, pp. 3575–3581, 2002.

[13] M. Belkin and P. Niyogi, "Laplacian eigenmaps for dimensionality reduction and data representation," *Neural Computation*, vol. 15, pp. 1373–1396, 2003.

[14] R. R. Coifman, S. Lafon, A.B. Lee, M. Maggioni, B. Nadler, F. Warner, and S.W. Zucker, "Geometric diffusions as a tool for harmonic analysis and structure definition of data: Diffusion maps," *Proceedings of the National Academy of Sciences*, vol. 102, no. 21, pp. 7426–7431, 2005.

[15] ——, "Geometric diffusions as a tool for harmonic analysis and structure definition of data: Multiscale methods," *Proceedings of the National Academy of Sciences*, vol. 102, no. 21, pp. 7432–7437, 2005.

[16] S. T. Roweis and L. K. Saul, "Nonlinear dimensionality reduction by locally linear embedding," *Science*, vol. 290, no. 5500, pp. 2323 – 2326, December 2000.

[17] J. B. Tenenbaum, V. de Silva, and J. C. Langford, "A global geometric framework for nonlinear dimensionality reduction," *Science*, vol. 290, no. 5500, pp. 2319 – 2323, December 2000.

[18] A. Singer, "From graph to manifold Laplacian: The convergence rate," *Applied and Computational Harmonic Analysis*, vol. 21, no. 1, pp. 128–134, July 2006.

[19] U. von Luxburg, O. Bousquet, and M. Belkin, "Limits of spectral clustering," in *Advances in Neural Information Processing Systems (NIPS) 17*, L. Saul, Y. Weiss, and L. Bottou, Eds. Cambridge, MA: MIT Press, 2005, pp. 857–864.

[20] B. Nadler, S. Lafon, R. R. Coifman, and I. Kevrekidis, "Diffusion maps, spectral clustering and eigenfunctions of Fokker-Planck operators," in *Advances in Neural Information Processing Systems 18*, Y. Weiss, B. Schölkopf, and J. Platt, Eds. Cambridge, MA: MIT Press, 2006, pp. 955–962.

[21] E. A. Coddington and N. Levinson, *Theory of Ordinary Differential Equations*. McGraw-Hill, 1984.

[22] H. A. David and H. N. Nagaraja, *Order Statistics*, 3rd ed. Wiley-Interscience, 2003.

[23] M. Hein and Y. Audibert, "Intrinsic dimensionality estimation of submanifolds in $\mathbb{R}^d$," in *Proceedings of the 22nd International Conference on Machine Learning*, L. De Raedt and S. Wrobel, Eds., 2005, pp. 289–296.

[24] M. Zakai and J. Ziv, "On the threshold effect in radar range estimation," *IEEE Transactions on Information Theory*, vol. 15, no. 1, pp. 167–170, 1969.

[25] J. Ziv and M. Zakai, "Some lower bounds on signal parameter estimation," *IEEE Transactions on Information Theory*, vol. 15, no. 3, pp. 386–391, 1969.

[26] L. P. Yaroslavsky, *Digital Picture Processing-An Introduction*. Berlin, Germany: Springer-Verlag, 1985.

[27] A. Buades, B. Coll, and J. M. Morel, "A review of image denoising algorithms, with a new one," *Multiscale Modeling & Simulation*, vol. 4, no. 2, pp. 490–530, 2005.

[28] A. D. Szlam, M. Maggioni, and R.R. Coifman, "A general framework for adaptive regularization based on diffusion processes on graphs," preprint.